information

Article

Generation of Synthetic Images of Trabecular Bone Based on Micro-CT Scans

Jonas Grande-Barreto [1], Eduardo Polanco-Castro [1], Hayde Peregrina-Barreto [2,*], Eduardo Rosas-Mialma [1] and Carmina Puig-Mar [1]

[1] Departamento de Ingeniería en Sistemas Computacionales, Universidad Politécnica Metropolitana de Puebla, Popocatépetl s/n, Reserva Territorial Atlixcáyotl, Tres Cerritos 72480, Mexico; jonas.grande@metropoli.edu.mx (J.G.-B.); eduardo.polanco@iberopuebla.mx (E.P.-C.); eduardo.2020110015@metropoli.edu.mx (E.R.-M.); carmina.2020110068@metropoli.edu.mx (C.P.-M.)
[2] Departamento de Ciencias Computacionales, Instituto Nacional de Astrofísica, Óptica y Electrónica, Luis Enrique Erro 1, Santa Maria Tonantzintla, San Andres Cholula 72840, Mexico
* Correspondence: hperegrina@inaoep.mx

Abstract: Creating synthetic images of trabecular tissue provides an alternative for researchers to validate algorithms designed to study trabecular bone. Developing synthetic images requires baseline data, such as datasets of digital biological samples or templates, often unavailable due to privacy restrictions. Even when this baseline is available, the standard procedure combines the information to generate a single template as a starting point, reducing the variability in the generated synthetic images. This work proposes a methodology for building synthetic images of trabecular bone structure, creating a 3D network that simulates it. Next, the technical characteristics of the micro-CT scanner, the biomechanical properties of trabecular bones, and the physics of the imaging process to produce a synthetic image are simulated. The proposed methodology does not require biological samples, datasets, or templates to generate synthetic images. Since each synthetic image built is unique, the methodology is enabled to generate a vast number of synthetic images, useful in the performance comparison of algorithms under different imaging conditions. The created synthetic images were assessed using microarchitecture parameters of reference, and experimental results provided evidence that the obtained values match approaches requiring initial data. The scope of this methodology covers research aspects related to using synthetic images in further biomedical research or the development of educational training tools to understand the medical image.

Keywords: synthetic image; micro-CT scan; trabecular bone; biomedicine; computer vision

Citation: Grande-Barreto, J.; Polanco-Castro, E.; Peregrina-Barreto, H.; Rosas-Mialma, E.; Puig-Mar, C. Generation of Synthetic Images of Trabecular Bone Based on Micro-CT Scans. *Information* **2022**, *14*, 375. https://doi.org/10.3390/info14070375

Academic Editor: Vincenzo Moscato

Received: 25 May 2023
Revised: 22 June 2023
Accepted: 28 June 2023
Published: 1 July 2023

1. Introduction

Medical imaging technologies, such as Dual-energy X-ray absorptiometry (DXA), high-resolution peripheral quantitative computed tomography (HR-pQCT), quantitative computed tomography (pQCT), and micro Computed Tomography (micro-CT) imaging, are the most effective approaches for assessing compartment-specific volumetric bone mineral density and bone microarchitecture in the peripheral skeleton [1]. In addition, the various medical image modalities for studying bone tissue provide information from different perspectives allowing detailed studies and discoveries in the area. For example, pathologies [2–4]; nutritional and pharmacologic treatments [5]; the impact of physical activity [6]; and fracture risk [7].

Most of the above investigations begin with a manual examination performed by clinical experts supported by a computational algorithm. The procedure attaches to the following structure: image conditioning, feature extraction, segmentation of bone tissue (trabecular or cortical), and finally, quantifying the bone tissue and its quality [8–10]. From a computational point of view, there is a continuing interest in developing algorithms that

outperform established algorithms. Therefore, it is necessary to test the algorithms on datasets with a broad diversity to determine the scope of established methods and propose improvements or new algorithms adapted to the current challenges. At this point, the computational part finds the first challenge since few bone databases include the bone microarchitecture ground truth (manual segmentation). Without this data, any algorithm demands validation by a clinical expert, who is not always available [11], and even so, a bias due to inter-classification can affect the validation process. Under these situations, synthetic images are an alternative to address the outline requirements.

Synthetic imaging comprises raw data (images) and ground truth (labels). Synthetic images can be configured according to a particular purpose. For example, adding different noise levels to raw data is helpful to test denoising algorithms [12], compare the segmentation accuracy of a set of algorithms related to bone segmentation [9], and detect microstructural features of trabecular bone [13]. Micro-CT is the medical imaging standard in scanners for acquiring trabecular bone samples because of the provided representation of the micro-structure size and image quality [8,14–17]. However, using these specialized scanners and preparing biological samples for digitization demands a high technical and clinical knowledge level that sometimes cannot be afforded. On the other hand, existing databases are not always available to conduct experiments. Therefore, the use of synthetic images is interesting for different experimental purposes.

The standard procedure for creating synthetic images involves the usage of a reference model, also known as a template. The template can be a digitized biological sample or a full-body phantom PBU-50 (Kyoto Kagaku Co., Ltd., Kyoto, Japan). It is possible to construct various synthetic images by modifying the template. A practical approach involves generating pseudo images from another imaging modality, such as Magnetic Resonance Imaging (MRI) [18,19]. The stereolithography approach manufactures trabecular bone models by printing 3D objects based on a layer-by-layer fabrication of structures defined by a numerical dataset [20,21]. Modifying pre-existing models by changing the voxel size, reconstruction algorithm, or adding a particular type of noise is a reliable approach for obtaining synthetic images [9]. Peña presented a novel method to generate synthetic images by combining the CT images from an anatomical model PBU-50 and a numerical algorithm [22]. According to the above, building clinical synthetic images should not be approached solely from a computational perspective. The algorithms or methodologies must have a direct or indirect relationship with the clinical part they try to simulate. For example, a direct relationship involves using real data to create a template. An indirect relationship could be using bioinspired algorithms that emulate a biological behavior generically.

The main limitation of most state-of-the-art approaches is that they require digitizing physical samples (real or phantom) to get an initial template. Therefore, building synthetic images of trabecular bone is challenging when base templates or public datasets are unavailable. This work proposes a computational method that combines graph networks and digital image processing to generate synthetic images of micro-CT trabecular bone with broad variability. The proposed method replaces the necessity of physical samples or pre-built templates by combining the small-world algorithm [23] and morphological operations. The simulated gray-level value was computed using the Beer–Lambert law; different types of noise were added to corrupt the generated images, simulating a more qualitatively natural representation of the trabecular structure [22]. The main contribution of this work is the proposed binary template model to produce 3D structures, simulating the architecture of trabecular bone. Unlike other methodologies addressing the same problem, the binary template model does not require a baseline of biological samples or templates. Each 3D structure built is unique, making it possible to set up a vast number of synthetic images to assess the scope of an algorithm and its performance comparison under different imaging conditions. The proposed methodology has a modular design that enables change blocks. For example, new research could use the proposed method but

change the projection model, conduct an experiment, and build synthetic images closer to the real ones.

This paper is structured as follows: Section 2 details the procedures required to create the synthetic image. Section 3 explains the experiment to build synthetic micro CT of trabecular bone, the obtained results, and a discussion. Finally, Section 5 contains the conclusion and future work.

2. Materials and Methods

In this paper, we start by describing the proposed methodology for generating synthetic micro-CT of trabecular bone. The modules that compose the procedure consist of a binary template model, a projection model, and noise addition. Figure 1 depicts the pipeline of the proposed method.

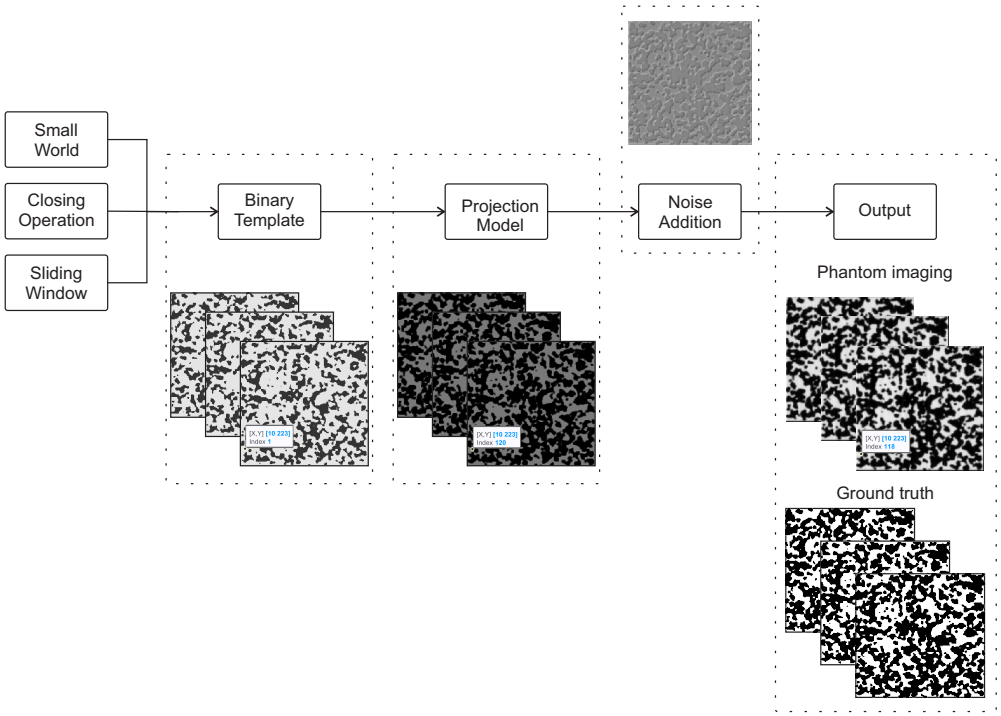

Figure 1. Pipeline of the proposed methodology.

2.1. Small-World Model

A small-world network, also known as the Watts–Strogatz (WS) model, refers to a regular ring graph composed of nodes that are connected to each other by edges [23]. The small-world network begins with a regular ring graph (Figure 2a), where all the nodes are connected to their four closest neighbors on the lattice. The WS model algorithm allows us to rewire a regular graph by introducing short-cut edges to connect distant nodes of the lattice (Figure 2b). The result of the modification is a graph of the small-world network family. Eventually, if the randomness level is further increased in a small-world network, the result is a purely quasi-random graph (Figure 2c). Then, a high randomness level reduces the probability that two lattices are equal, which is a desired behavior since the variety of trabecular structures to be simulated is increased.

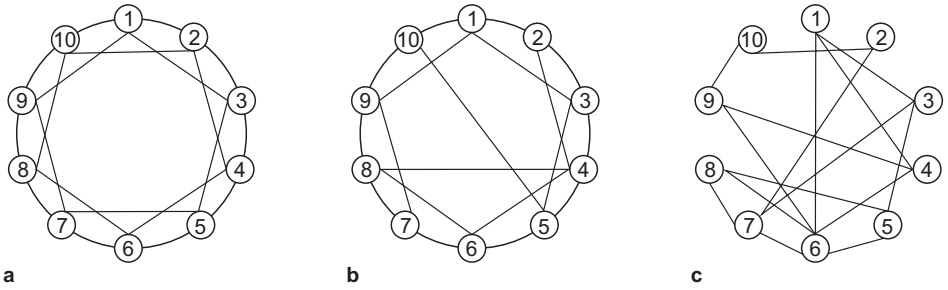

Figure 2. Network graphs generated by the WS model. (**a**) The network is a regular lattice. (**b**) A small-world network is created when some edges are modified. (**c**) The modification of a high percentage of edges leads to a random graph.

2.2. Closing Operation

Mathematical transformations are based on geometry and set theory. These types of operations are often used to highlight/attenuate the size or shape of elements (structures) in the image [24]. A morphological transformation $\Psi(f)$ is an operation that considers the value of a current pixel in image f and its surroundings to be transformed by an operator given a morphological reference. This means that f is defined by the relationship between a subset of pixels from f and the values of another set of the same size B known as the structuring element (SE). The shape or morphology defined by B is often square, circular, linear, or hexagonal. Although there is no restriction with regards to the morphology of B, being adapted in specific applications, the most-used morphology is square. Then, $B\lambda$ defines as a square of $(2\lambda + 1) \times (2\lambda + 1)$ where λ is the size of the transformation affecting image f. Commonly, when a transformation has size $\lambda = 1$, this is indicated as $\Psi_{B\lambda}(f)$ or just $\Psi(f)$.

To perform a morphological transformation, the origin (center) of B must overlap with the current pixel of the image $f(x)$. Then, B analyzes all the underlying image pixels in f through Ψ. Morphological dilation and erosion are fundamental morphological operations. In the numerical case (gray level images), dilation is defined as $\delta_{B\lambda}(f) = max\{f(y)|y \in \lambda B\}$, and erosion as $\varepsilon_{B\lambda}(f) = min\{f(y)|y \in \lambda B\}$. Dilation allows regions at a distance $B\lambda$ to be connected while erosion increases their distance in a scale $B\lambda$. Morphological opening $\gamma_{B\lambda}(f) = \delta_{B\lambda}[\varepsilon_{B\lambda}(f)]$, and closing $\sigma_{B\lambda}(f) = \varepsilon_{B\lambda}[\delta_{B\lambda}(f)]$ are composed morphological transformations, where the aim of the first operation is to connected/disconnected regions [25]. To avoid the distortion generated in the structures by the first operation, the dual operation is applied next, trying a restoration process. However, it must be considered that dual operation does not cancel the effect in the connection/disconnection of regions; it only tries to restore the area of the remaining regions.

2.3. Binary Template Model

Bone trabecular structures represent a quasi-random network based on a structure of interconnected plates and rods. Generating a simulated micro-architecture requires a combination of surfaces and curves through a numerical model. If the developed model bypasses biological constraints, the result is somewhat unlike that observed in clinical images. The main limitation of the WS algorithm for the goal of this research is that the lattices generated are in 2D, while a 3D lattice is required to represent the structure of the trabecular bone. Furthermore, the WS model does not consider network growth [26]. It implies a fixed number of nodes and does not allow the network to grow over time. On the other hand, if we try to stack the 2D lattices to create a 3D lattice, the natural structure of the trabecular bone will not be represented because the 2D lattices are different, and stacking them will compromise the continuity of the synthetic trabecular bone built. Therefore, using only the WS model to generate synthetic images of trabecular bone is not recommended because of the outlined limitations. We address this limitation by including a voting strategy to combine the 2D lattices and create a 3D structure that effectively represents the trabecular bone structure.

Using the WS model algorithm, the process begins by creating k binary images (SW) of size $m \times n$. The algorithm behavior ensures that no image is replicated. The k SW images are stacked with a sliding window over them. A sliding window is a rectangular region that slides across an image with a fixed width, height, and depth to compute an operation over the area covered. Then, to determine if the pixel in the position $S(x, y, z)$ is inter-trabecular space (0) or trabecular bone (1), a sliding window Ω of size $(\omega \times \omega \times k)$ places on the k SW images in the position $SW(x, y)$. Finally, the decision is made using the following equation:

$$S(x,y,z) = \begin{cases} 1 & \frac{\sum_1^k \sum_{l \in \Omega}(SW_k = 1)}{\sum_1^k \sum_{l \in \Omega}(SW_k)} \geq \tau \\ 0 & \text{otherwise} \end{cases} \quad (1)$$

where $S(x, y, z)$ represents the pixel's value in the position (x, y, z), l represents pixels in Ω, and rho is a threshold parameter that controls the density of pixels with $SW_k = 1$. Figure 3 depicts the process for generating a binary template S with size $m \times n \times v$. For example, in Figure 3 with $p = 0.3$ and $\omega = 5$, the pixel in position $S(a, b, z)$ is set as trabecular bone (1) because $\frac{23}{75} \geq 0.3$. On the other hand, the pixel in position $S(c, d, z)$ is set as inter-trabecular space (0) because $\frac{13}{75} < 0.3$. The outlined process repeats for all the positions of the stacked images. In order to enhance the resulting 3D structure, a morphological closing operation is applied to the image. We suggest alternating the structuring element for closing operation to preserve the natural structure of the trabecular bone, avoiding this manner predictable pattern. The result of the proposed binary template model is a 3D structure that simulates the distribution of trabecular bone in a biological sample but with the advantage of not needing a dataset or template as a baseline. This point highlights the proposed method because it is possible to generate two types of synthetic data, printed rigid synthetic cellular polyurethane bones for mechanical tests [27] or, as this research proposes, use them to build synthetic images of trabecular bone. We developed a binary bone template inspired by biological and quasi-random graphs using the WS model and a voting strategy.

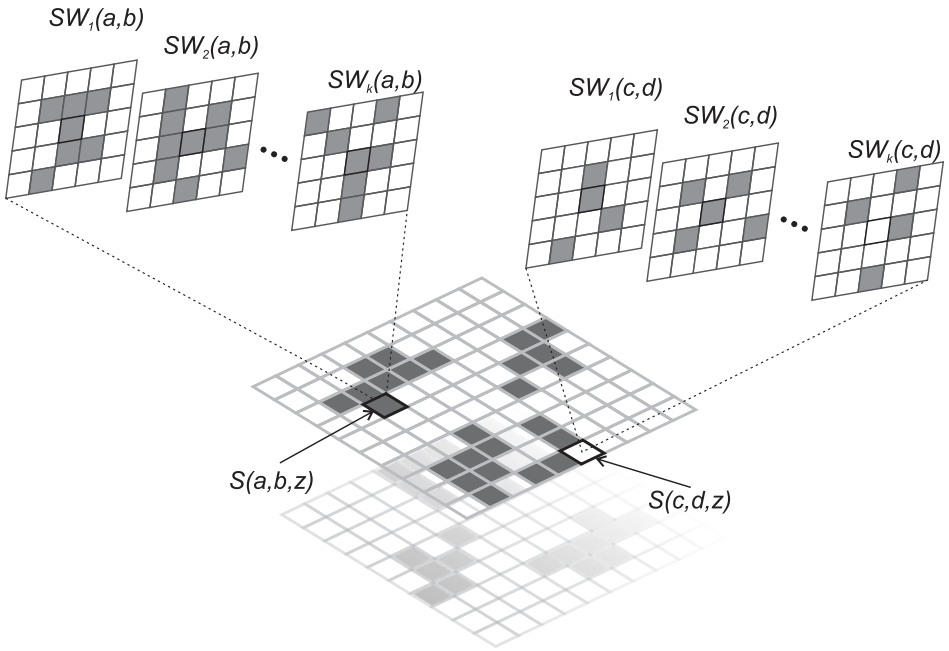

Figure 3. Building of a binary template. The inter-trabecular space pixels are depicted in white, while the trabecular bone pixels are in gray. The pixel (a, b) is labeled trabecular bone due to the high density of gray pixels in the Ω neighborhood of SW images. In contrast, pixel (c, d) is labeled as inter-trabecular space due to the low Ω neighborhood density of gray pixels in SW images.

2.4. Projection Model

At this stage, the binary template model contains structural information about the distribution of trabecular bone and inter-trabecular space pixels. The binary template model does not include information about the gray-level pixel distribution. According to the Beer–Lambert law, the light attenuation through a medium is proportional to the concentration of the light absorbers present in the substance, the optical properties of the light absorber, and the optical path length traveled by the light beam [28]. We use the model proposed by [29] to assign a gray-level value $P(x, y)$ of each point p at the coordinated (x, y) in the simulated projection image using the following equation:

$$P(x, y) = I_0 \cdot e^{-\mu \cdot \sum_{z=1}^{N_z} S(x,y,z)} \quad (2)$$

where:

P is the 2D image selected from the volume.
$P(x, y)$ is the pixel value at the (x, y) coordinates within the grayscale.
S is the 3D image with binary values.
$S(x, y, z)$ is the binary value (0 =inter-trabecular space, 1 =trabecular bone) of the pixel in the coordinates (x, y, z) at S.
N_z is the projection thickness (size of S following the z-axis).
μ is the bone attenuation coefficient (cm^{-1}).
I_0 is the X-ray energy of the photons in kilo-electron volt (KeV).

Considering a bone density of 1.65 cm^3, it is proposed to use 100 and 150 KeV values for the X-ray energy and an attenuation coefficient of 0.08 and 0.05 cm^{-1}, respectively [29]. The principle of operation of Equation (2) establishes that if in a specific spot of the 3D binary template stand a large number of white pixels (bone), then the attenuation factor increases its value for a particular location. Therefore, the gray level for $P(x, y)$ is close to 255 when the summation result is greater than 0, and vice versa. The outlined model is applied to every image in the binary template model to generate synthetic micro-CT of trabecular bone. It is necessary to point out that the projection model outlined provides an estimation of the gray-level distribution. Compared with the results from CT scanners, the gray-level distribution will differ because of the refinement processes integrated into the CT scanners.

2.5. Adding Noise

The output of the projection model is a synthetic micro-CT of trabecular bone which does not include relevant artifacts such as noise. The state-of-the-art indicates that the Gaussian white noise in micro-CT is the most common. Therefore, we corrupted all the images with Gaussian white noise. According to the state-of-the-art [9,29,30], it is recommended to use values from 0.1 (better case) to 0.9 (worst case) of standard deviation (SD) to configure the white noise for the case of computer tomographies.

3. Experimental Results

The goal of the experiment is to generate synthetic micro-CT of trabecular bone. The experimental hypothesis states that a methodology based on a binary template model, projection model, and noise addition can generate synthetic trabecular bone micro-CT images. The proposed method was developed in MATLAB 2022b. Table 1 describes the parameters and their values used in the experiment. We generate 20 synthetic images, 10 with $\rho = 0.35$ and 10 with $\rho = 0.38$, to analyze the effect of ρ in the image formation process. We use default parameters for a small-world algorithm [23].

Table 1. Experimental set-up.

Parameter	Value	Description
Binary template model		
[X Y Z]	[256 256 150]	Dimension of the synthetic image
ρ	[0.35, 0.38]	Controls the pixel template density
Ω	[5 5 10]	Size of the sliding window
Projection model		
μ	0.39	Bone attenuation coefficient
I_0	120	X-ray energy
N_z	[3 3 3]	Projection thickness
Voxel size		
Isotropic voxel: 1000 µm		

Figure 4 compares a set of slices from two different volumes using $\rho = 0.35$ and $\rho = 0.38$ in three consecutive slices (z-axis). For the top row, in the region of interest (ROI) #1 in slice $z - 1$, it is possible to appreciate a trabecula gap that changes over the successive slices until the gap closes. In ROI #2 ($z - 1$), an isolated section of trabecular bone enlarges its surface (z) until it joins with a main trabecular bone section (z + 1). Finally, ROI #3 depicts how another main area of trabecular bone changes through the slices and covers a larger surface. The bottom row presents exciting results. ROI #1 ($z - 1$) depicts how the trabecular structure changes to fill an inter-trabecula section. The change is soft but does not follow predictable behavior. ROI #2 shows how the inter-trabecula moves in the trabecular bone to create structural gaps. Finally, ROI #3 shows a change in the form of a section of an isolated inter-trabecula section.

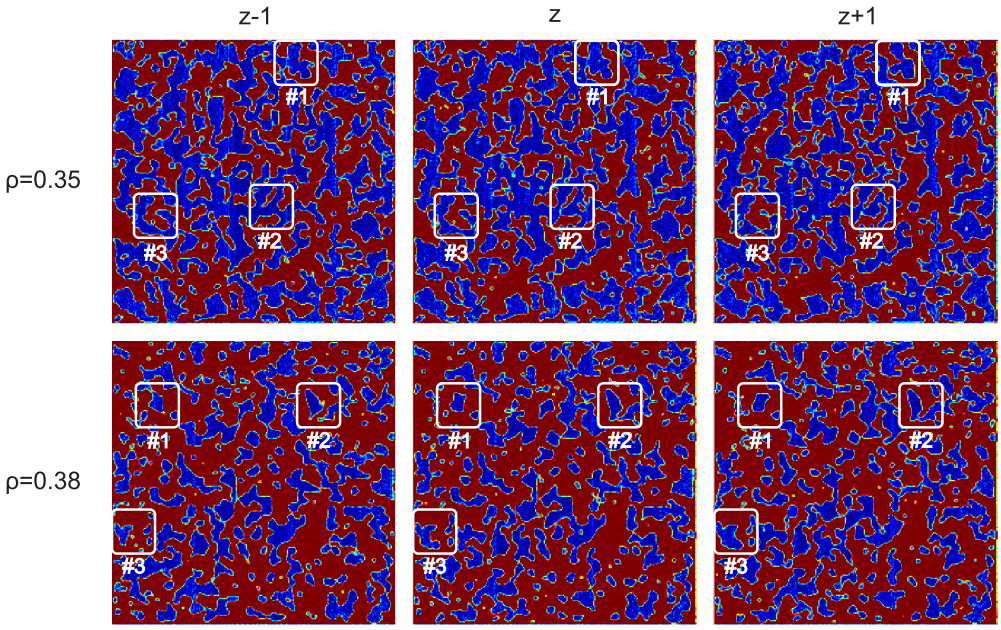

Figure 4. Three consecutive synthetic micro-CT slices of trabecular bone with different densities. A gradual shift between trabecular bone (red) and inter-trabecula space (blue) can be observed within the ROIs in each image. Pixels in green-yellow represent the partial volume effect.

This change also illustrates that two regions do not follow the same modifications, i.e., even when both regions grow, they will do it in a different direction, size, or timing. The outlined behavior is present not only on the z-axis but also on the x-axis and y-axis. Figure 5 depicts volumetric data along slice planes orthogonal to each axis. From different views, it is possible to observe how the trabecular bone structure is continuous in each plane and interconnects between planes. The results show that changes occur gradually from one

slice to another. It also shows no predictable pattern in the modifications suffered by the trabecular bone structure. Figure 6a shows a 3D representation of a synthetic micro-CT. In the image, it is possible to observe the trabecular bone structure from a volumetric view. Figure 6b shows the interior of the 3D-printed synthetic micro-CT of trabecular bone. An interconnection of plates and rods supports the trabecular bone structure.

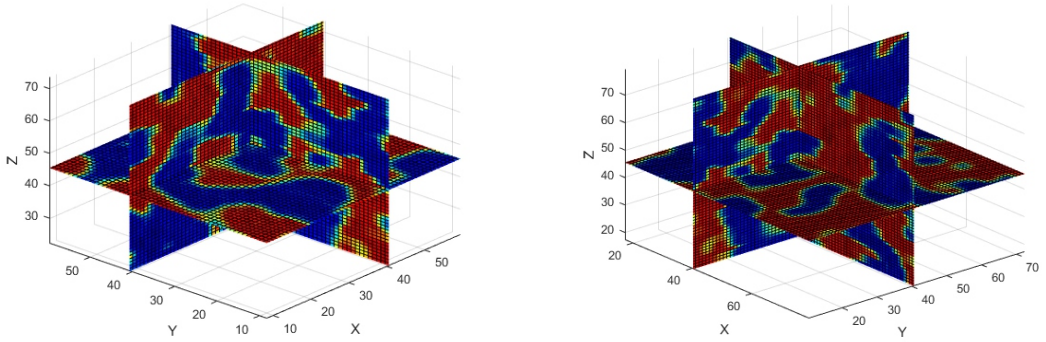

a **b**

Figure 5. Micro-CT of trabecular bone viewed from orthogonal planes, (**a**) depicts a synthetic image with $\rho = 0.35$, (**b**) depicts a synthetic image with $\rho = 0.38$.

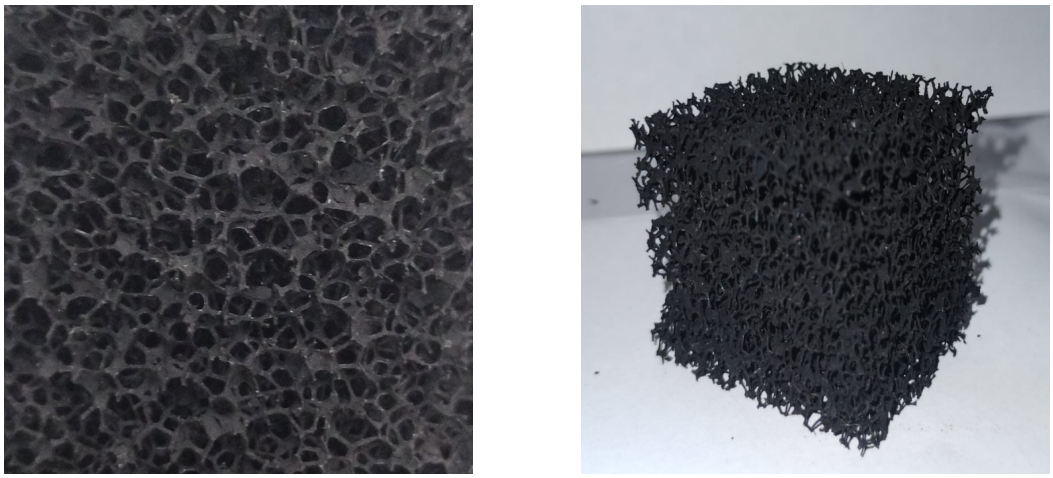

a **b**

Figure 6. Volumetric synthetic micro-CT of trabecular bone, (**a**) depicts a printed single layer of the synthetic image, (**b**) depicts a printed whole volume of synthetic micro-CT of trabecular bone.

In order to perform a quantitative evaluation of the synthetic images built, we computed microarchitecture parameters. The computation of these parameters is performed using stereological techniques and under the assumption that the bone sample has a microstructure composed of plates or rods [31].

The formulations of equations to compute microarchitecture parameters were developed initially for conventional histomorphometry and continue to be used in 2D micro-CT analysis. In this study, three primary parameters were assessed to calculate microarchitecture parameters: bone volume (BV), bone surface area (BS), and tissue volume (TV). Thus, the following parameters are determined:

- Bone volume fraction/density (BV/TV) is the volume of mineralized bone per unit volume of the sample. BV/TV is simply the number of foreground (bone) voxels divided by the total number of voxels in the image. The measurement unit is %.
- Trabecular Thickness (Tb.Th) is the trabeculae's average thickness. The measurement unit is mm or μm.

- Trabecular Separation (Tb.Sp) is the main diameter of the bone marrow cavities. The measurement unit is mm or μm.

We used BoneJ [32] to compute the trabecular microarchitecture parameters to assess the synthetic images built quantitatively. The described parameters are the minimal set that should be reported when describing trabecular bone morphology [15]. Table 2 shows related research that addressed the creation of synthetic micro-CT of trabecular bone and the microarchitecture parameters used to describe the synthetic trabecular bone structure [1]. Since the approaches to the problem are diverse, we analyzed the input data and the metrics used to know the structural conditions of synthetic micro-CT of trabecular bone. Current works require reference data such as biological samples, datasets, or templates as a starting point for generating synthetic samples. As more information integrates into the model, the synthetic images will be closer to a real ones. Nevertheless, only one data type is available in most cases. In addition, due to the lack of available reference databases, each study works with private data and different anatomical references (human and animal). The proposed methodology does not require prior information because it uses biological small-world networks that simulate the quasi-random structure of interconnected plates and rods that characterize the trabecular bone. Therefore, the output is a generic trabecular structure, helpful as a first assessment tool for new algorithms focused on trabecular bone segmentation.

Table 2. Microarchitecture parameters computed from the synthetic micro-CT of trabecular bone.

Author	Required Information			Anatomical Reference	Metric
	Biological	Dataset	Template		
Ho et al. [27]	No	No	Yes	Human dental	BV/TV = 0.36 ± 0.11 Tb.Th = 31 ± 1 μm Tb.Sp = 71 ± 5 μm
Winzenrieth et al. [29]	Yes	Yes	No	Human vertebrae	BV/TV = 0.29 ± 0.05 Tb.Th = 23 ± 2 μm Tb.Sp = 53 ± 13 μm
Pena et al. [22]	Yes	No	Yes	Human ulna Human vertebrae	Tb.Th = 15 ± 7 μm Tb.Th = 22 ± 9 μm
Xiao et al. [13]	No	No	Yes	Human femur Human femur	BV/TV = 0.29 ± 0.15 Tb.Th = 28 ± 13 μm BV/TV = 0.08 ± 0.05 Tb.Th = 16 ± 3 μm
Proposed	No	No	No	Generic ($\rho = 0.35$) Generic ($\rho = 0.38$)	BV/TV = 0.38 ± 0.01 Tb.Th = 12 ± 9 μm Tb.Sp = 12 ± 11 μm BV/TV = 0.53 ± 0.02 Tb.Th = 23 ± 2 μm Tb.Sp = 21 ± 2 μm

From Table 2, it is observed that even using anatomical references, microarchitecture parameters reported in previous works present wide dispersion. The values reported for BV/TV show that bone mass changes depending on the anatomical reference used. In the proposed methodology, the ρ value controls the BV/TV value; low ρ values correspond to low BV/TV values and vice versa. For Tb.Th, authors reported low values from 16 ± 3 to 31 ± 1 μm; on the other hand, Tb.Sp values presented higher values from 53 ± 13 to 71 ± 5 μm. The synthetic images created with the proposed methodology reported values for Tb.Th o Tb.Sp that are in the range of the current works reported. The distinctive feature of the images created is the relationship between Tb.Th and Tb.Sp, having both parameters a linear correspondence and changing proportionally when ρ varies. This effect is because the degree distribution of a network graph generated with the WS model is relatively homogeneous. Therefore, the proposed methodology balances the amount of trabecular bone and the cavities containing the bone marrow.

4. Discussion

Synthetic images provide ground truth to measure the performance of image processing algorithms (denoising and segmentation) for validation or exploratory studies. The experimental results show evidence that the proposed methodology can generate synthetic images based on micro-CT of trabecular bone. The synthetic images generated produce a trabecular bone structure based on a quasi-random grid based on interconnected plates and rods based on mathematical models. This condition is a key point in our methodology because it is not based on a particular type of bone but on a relationship of biological and mathematical constraints. Strictly speaking, the proposed methodology is a proof of concept that produces generic synthetic micro-CT of trabecular bone.

The main contribution of the proposed work is creating a generic 3D structure that simulates the architecture of trabecular bone without requiring initial biological samples. Often, in methodologies based on biological samples, the quantity and variety of synthetic images are limited because of the need for sizeable trabecular bone datasets. We addressed the outlined problem allowing the user to set the amount of bone, spatial resolution, and percentage of noise in the image. Therefore, algorithms interested in analyzing the structural characteristics of trabecular bone will be able to carry out tests with a wide variety of synthetic image configurations. For example, the starting point for these analyses is a binary image obtained from the raw image, so synthetic images help to validate new algorithms focused on segmenting trabecular bone [9,33]. Moreover, the proposed methodology does not repeat 3D structures through the binary template, ensuring that all generated images will be unique. This point is critical since new methods, e.g., based on deep learning, could be applied to analyze this type of image to find new representations or relationships that help to differentiate healthy patients from those associated with some pathology. It is important to point out that experiments related to pathologies are out of the scope of the proposed methodology for now. Nevertheless, the assessment of pathologies related to trabecular bone volume reduction is a task that can be simulated.

Regarding the modular design of the proposed methodology, there are several points for improvement. We found limitations with the WS model for the binary template model. The most important is that it does not allow the network to grow over time. The Barabási–Albert model (or simply the BA model) is a potential candidate since it produces a similar result to the WS model but supports network growth [34]. We chose a straightforward model to implement for the projection model, obtaining competitive results. We consider, in future work, comparing different projection models in order to find which model produces gray-level distribution closest to real micro-CT of trabecular bone. We consider exploring the projection model proposed in [31] as a first option. Concerning the image artifacts, we considered including other perturbations into the synthetic images in order to build a more realistic synthetic micro-CT of trabecular bone. The first artifact to include is the ring artifact that looks similar to rings or half rings around the rotation center of the reconstructed image. The second is the partial-volume effect, described as the mixture of signals of different objects due to poor spatial resolution. Finally, in future work, we consider extending the proposed methodology to simulate the structure of trabecular bone from a specific location in the human skeleton by incorporating real images into the model using image fusion [35].

5. Conclusions

This paper presents a novel methodology that generates synthetic micro-CT of trabecular bone. The procedure integrates a new binary template model, projection model, and noise to create synthetic images. The binary template model is the main contribution of the research because it can generate a 3D structure that simulates trabecular bone architecture. Furthermore, the binary template model is free of biological samples, datasets, or baseline templates. This condition is a highlight because it is possible to create a wide range of synthetic images. Because the created images are artificial, they are generic and do not represent a particular type of trabecular bone. Still, the microarchitecture parameters

computed are in the range of those reported by current works that used biological dataset baselines. Therefore, the data generated present an exciting challenge to validate algorithms related to the study of trabecular bone. Current works in the field provide evidence of the interest and competition for developing methodologies capable of constructing synthetic micro-CT of trabecular bone. To conclude the study, the modular design of the proposed methodology would allow it to replace or integrate other blocks to carry out new experiments and generate new knowledge.

Author Contributions: Investigation, J.G.-B. and H.P.-B.; methodology, J.G.-B. and E.P.-C.; supervision, H.P.-B. and C.P.-M.; writing—original draft, J.G.-B.; writing—review-editing, J.G.-B. and E.R.-M. All authors have read and agreed to the published version of the manuscript.

Funding: This research received no external funding.

Informed Consent Statement: Not applicable.

Data Availability Statement: Not applicable.

Conflicts of Interest: The authors declare no conflicts of interest.

References

1. Whittier, D.E.; Boyd, S.K.; Burghardt, A.J.; Paccou, J.; Ghasem-Zadeh, A.; Chapurlat, R.; Engelke, K.; Bouxsein, M.L. Guidelines for the assessment of bone density and microarchitecture in vivo using high-resolution peripheral quantitative computed tomography. *Osteoporos. Int.* **2020**, *31*, 1607–1627. [CrossRef] [PubMed]
2. Nour, M.A.; Burt, L.A.; Perry, R.J.; Stephure, D.K.; Hanley, D.A.; Boyd, S.K. Impact of growth hormone on adult bone quality in Turner syndrome: A HR-pQCT study. *Calcif. Tissue Int.* **2016**, *98*, 49–59. [CrossRef]
3. Braun, C.; Bacchetta, J.; Braillon, P.; Chapurlat, R.; Drai, J.; Reix, P. Children and adolescents with cystic fibrosis display moderate bone microarchitecture abnormalities: Data from high-resolution peripheral quantitative computed tomography. *Osteoporos. Int.* **2017**, *28*, 3179–3188. [CrossRef] [PubMed]
4. Samelson, E.J.; Demissie, S.; Cupples, L.A.; Zhang, X.; Xu, H.; Liu, C.T.; Boyd, S.K.; McLean, R.R.; Broe, K.E.; Kiel, D.P.; et al. Diabetes and deficits in cortical bone density, microarchitecture, and bone size: Framingham HR-pQCT study. *J. Bone Miner. Res.* **2018**, *33*, 54–62. [CrossRef] [PubMed]
5. Burt, L.A.; Billington, E.O.; Rose, M.S.; Raymond, D.A.; Hanley, D.A.; Boyd, S.K. Effect of high-dose vitamin D supplementation on volumetric bone density and bone strength: A randomized clinical trial. *JAMA* **2019**, *322*, 736–745. [CrossRef]
6. Burt, L.A.; Schipilow, J.D.; Boyd, S.K. Competitive trampolining influences trabecular bone structure, bone size, and bone strength. *J. Sport Health Sci.* **2016**, *5*, 469–475. [CrossRef] [PubMed]
7. Mikolajewicz, N.; Bishop, N.; Burghardt, A.J.; Folkestad, L.; Hall, A.; Kozloff, K.M.; Lukey, P.T.; Molloy-Bland, M.; Morin, S.N.; Offiah, A.C.; et al. HR-pQCT measures of bone microarchitecture predict fracture: Systematic review and meta-analysis. *J. Bone Miner. Res.* **2020**, *35*, 446–459. [CrossRef] [PubMed]
8. Abid Fourati, W.; Bouhlel, M.S. Trabecular bone image segmentation using wavelet and marker-controlled watershed transformation. *Chin. J. Eng.* **2014**, *2014*. [CrossRef]
9. Engelkes, K. Accuracy of bone segmentation and surface generation strategies analyzed by using synthetic CT volumes. *J. Anat.* **2021**, *238*, 1456–1471. [CrossRef]
10. Euler, A.; Nowak, T.; Bucher, B.; Eberhard, M.; Schmidt, B.; Flohr, T.G.; Frey, D.; Distler, O.; Alkadhi, H. Assessment of bone mineral density from a computed tomography topogram of photon-counting detector computed tomography—Effect of phantom size and tube voltage. *Investig. Radiol.* **2021**, *56*, 614–620. [CrossRef]
11. Caron, R.; Londono, I.; Seoud, L.; Villemure, I. Segmentation of trabecular bone microdamage in Xray microCT images using a two-step deep learning method. *J. Mech. Behav. Biomed. Mater.* **2023**, *137*, 105540. [CrossRef] [PubMed]
12. Diwakar, M.; Kumar, M. A review on CT image noise and its denoising. *Biomed. Signal Process. Control.* **2018**, *42*, 73–88. [CrossRef]
13. Xiao, P.; Zhang, T.; Dong, X.N.; Han, Y.; Huang, Y.; Wang, X. Prediction of trabecular bone architectural features by deep learning models using simulated DXA images. *Bone Rep.* **2020**, *13*, 100295. [CrossRef] [PubMed]
14. Stauber, M.; Müller, R. Micro-computed tomography: A method for the non-destructive evaluation of the three-dimensional structure of biological specimens. In *Osteoporosis*; Springer: Berlin/Heidelberg, Germany, 2008; pp. 273–292.
15. Bouxsein, M.L.; Boyd, S.K.; Christiansen, B.A.; Guldberg, R.E.; Jepsen, K.J.; Müller, R. Guidelines for assessment of bone microstructure in rodents using micro–computed tomography. *J. Bone Miner. Res.* **2010**, *25*, 1468–1486. [CrossRef] [PubMed]
16. Christiansen, B.A. Effect of micro-computed tomography voxel size and segmentation method on trabecular bone microstructure measures in mice. *Bone Rep.* **2016**, *5*, 136–140. [CrossRef]
17. Ryan, M.; Barnett, L.; Rochester, J.; Wilkinson, J.; Dall'Ara, E. A new approach to comprehensively evaluate the morphological properties of the human femoral head: Example of application to osteoarthritic joint. *Sci. Rep.* **2020**, *10*, 5538. [CrossRef]

18. Hsu, S.H.; Cao, Y.; Huang, K.; Feng, M.; Balter, J.M. Investigation of a method for generating synthetic CT models from MRI scans of the head and neck for radiation therapy. *Phys. Med. Biol.* **2013**, *58*, 8419. [CrossRef]
19. Sjölund, J.; Forsberg, D.; Andersson, M.; Knutsson, H. Generating patient specific pseudo-CT of the head from MR using atlas-based regression. *Phys. Med. Biol.* **2015**, *60*, 825. [CrossRef]
20. Mézière, F.; Juskova, P.; Woittequand, J.; Muller, M.; Bossy, E.; Boistel, R.; Malaquin, L.; Derode, A. Experimental observation of ultrasound fast and slow waves through three-dimensional printed trabecular bone phantoms. *J. Acoust. Soc. Am.* **2016**, *139*, EL13–EL18. [CrossRef]
21. Grzeszczak, A.; Lewin, S.; Eriksson, O.; Kreuger, J.; Persson, C. The Potential of Stereolithography for 3D Printing of Synthetic Trabecular Bone Structures. *Materials* **2021**, *14*, 3712. [CrossRef]
22. Peña-Solórzano, C.A.; Albrecht, D.W.; Paganin, D.M.; Harris, P.C.; Hall, C.J.; Bassed, R.B.; Dimmock, M.R. Development of a simple numerical model for trabecular bone structures. *Med. Phys.* **2019**, *46*, 1766–1776. [CrossRef]
23. Watts, D.J.; Strogatz, S.H. Collective dynamics of 'small-world'networks. *Nature* **1998**, *393*, 440–442. [CrossRef]
24. Serra, J.; Soille, P. *Mathematical Morphology and Its Applications To Image Processing*; Springer Science & Business Media: Berlin/Heidelberg, Germany, 2012; Volume 2.
25. Haralick, R.M.; Sternberg, S.R.; Zhuang, X. Image analysis using mathematical morphology. *IEEE Trans. Pattern Anal. Mach. Intell.* **1987**, *PAMI-9*, 532–550. [CrossRef]
26. Arnaboldi, V.; Passarella, A.; Conti, M.; Dunbar, R.I. *Online Social Networks: Human Cognitive Constraints in Facebook And Twitter Personal Graphs*; Elsevier: Amsterdam, The Netherlands, 2015.
27. Ho, J.T.; Wu, J.; Huang, H.L.; Chen, M.Y.; Fuh, L.J.; Hsu, J.T. Trabecular bone structural parameters evaluated using dental cone-beam computed tomography: Cellular synthetic bones. *Biomed. Eng. Online* **2013**, *12*, 115. [CrossRef]
28. Narayan, R. *Encyclopedia of Biomedical Engineering*; Elsevier: Amsterdam, The Netherlands, 2018.
29. Winzenrieth, R.; Michelet, F.; Hans, D. Three-Dimensional (3D) Microarchitecture Correlations with 2D Projection Image Gray-Level Variations Assessed by Trabecular Bone Score Using High-Resolution Computed Tomographic Acquisitions: Effects of Resolution and Noise. *J. Clin. Densitom.* **2013**, *16*, 287–296. [CrossRef]
30. Jiang, H. *Computed Tomography: Principles, Design, Artifacts, and Recent Advances*; SPIE and John Wiley & Sons, Inc.: Bellingham, WA, USA, 2009.
31. da Silva, A.M.H.; Alves, J.M.; da Silva, O.L.; da Silva Junior, N.F. Two and three-dimensional morphometric analysis of trabecular bone using X-ray microtomography (μCT). *Rev. Bras. Eng. Biomed* **2014**, *30*, 93–101. [CrossRef]
32. Doube, M.; Kłosowski, M.M.; Arganda-Carreras, I.; Cordelières, F.P.; Dougherty, R.P.; Jackson, J.S.; Schmid, B.; Hutchinson, J.R.; Shefelbine, S.J. BoneJ: Free and extensible bone image analysis in ImageJ. *Bone* **2010**, *47*, 1076–1079. [CrossRef]
33. Chegeni, N.; Birgani, M.J.T.; Birgani, F.F.; Fatehi, D.; Akbarizadeh, G.; Tahmasbi, M. Introduction of a simple algorithm to create synthetic-Computed tomography of the head from magnetic resonance imaging. *J. Med. Signals Sens.* **2019**, *9*, 123. [PubMed]
34. Onnela, J.P.; Saramäki, J.; Hyvönen, J.; Szabó, G.; Lazer, D.; Kaski, K.; Kertész, J.; Barabási, A.L. Structure and tie strengths in mobile communication networks. *Proc. Natl. Acad. Sci. USA* **2007**, *104*, 7332–7336. [CrossRef] [PubMed]
35. Liu, S.; Huang, S.; Wang, S.; Muhammad, K.; Bellavista, P.; Del Ser, J. Visual tracking in complex scenes: A location fusion mechanism based on the combination of multiple visual cognition flows. *Inf. Fusion* **2023**, *96*, 281–296. [CrossRef]